Multistable sheets with rewritable patterns for switchable shape-morphing

Meeussen, A.S.; Hecke, M.L. van

Article

Multistable sheets with rewritable patterns for switchable shape-morphing

https://doi.org/10.1038/s41586-023-06353-5

Received: 18 October 2022

Accepted: 21 June 2023

Published online: 20 September 2023

Check for updates

A. S. Meeussen[1,2,3] ✉ & M. van Hecke[1,2]

Flat sheets patterned with folds, cuts or swelling regions can deform into complex three-dimensional shapes under external stimuli[1–24]. However, current strategies require prepatterning and lack intrinsic shape selection[5–24]. Moreover, they either rely on permanent deformations[6,12–14,17,18], preventing corrections or erasure of a shape, or sustained stimulation[5,7–11,25], thus yielding shapes that are unstable. Here we show that shape-morphing strategies based on mechanical multistability can overcome these limitations. We focus on undulating metasheets that store memories of mechanical stimuli in patterns of self-stabilizing scars. After removing external stimuli, scars persist and force the sheet to switch to sharply selected curved, curled and twisted shapes. These stable shapes can be erased by appropriate forcing, allowing rewritable patterns and repeated and robust actuation. Our strategy is material agnostic, extendable to other undulation patterns and instabilities, and scale-free, allowing applications from miniature to architectural scales.

The transformation of flat sheets into three-dimensional (3D) shapes is fundamental in nature, science and technology. Patterns of shrinking and stretching underlie the wrinkling of leaves, skin and torn plastic sheets, as well as the reshaping of lettuce leaves and organ tissue[1–4]. These processes have inspired shape-morphing strategies for man-made sheets that shrink or grow under light, heat, pressure or chemical stimuli[5–11]. Likewise, purely geometric origami- and kirigami-based strategies leverage patterns of folds and cuts for the formation of 3D shapes[12–16]. Together, these strategies yield applications ranging from self-folding robots to smart actuators and microelectromechanical systems (MEMS)[17–22]. Ideal shape-morphing strategies are simple and yield a variety of stable and precisely selected 3D shapes. However, current strategies require complex prepatterning of the sheet (with cuts, folds, optical markers, swelling regions, pre-stress or director fields)[5–24]. Moreover, strategies based on reversible actuation produce shapes that relax when the stimulus is removed[5,7–11,25], whereas strategies based on irreversible deformations are prone to overshooting[6,12–14,17,18]. This provokes the question: are there robust shape-morphing strategies that inherently combine stability and selectivity? Here, we leverage multistability to address this challenge. To demonstrate the power of multistability, we introduce the specific class of groovy metasheets as a new shape-morphing platform that allows repeated switching from the flat state to multiple, precisely selected and stable 3D shapes.

Our metasheets are thin sheets embossed with patterns of parallel grooves, reminiscent of corrugated plate materials (Fig. 1a,b; Methods) whose high effective stiffness-to-density ratio have made them desirable construction materials and subject of extensive research[25]. These metasheets morph via a two-step process. In the first step, stretching with point forces induces hallmark snap-through defects in each groove (Fig. 1c; Methods). Under continued forcing, these multistable defects self-organize into a scar (Fig. 1d). Scar formation is robust and insensitive to perturbed or excess forcing, and produces the building blocks of our reshaping patterns. In the second step, external forces are removed. Away from the scar, the sheet aims to relax to its unstressed state; however, the scar remains, encoding local stretching and forcing the metasheet to reproducibly switch to a precise 3D shape (Fig. 1e) that is stable to perturbations (Fig. 1f). Applying a suitable strong flattening force erases the pattern and returns the metasheet to its initial state (Fig. 1g). Vitally, the grooves allow effective stretching of the metasheet without plastic stretching of the constituent material, provided the groove's radius r and thickness t and the material's Young's modulus E and yield strength σ_y obey the relation $\frac{R}{t} > \frac{E}{2\sigma_y}$, as is the case here; consequently, minimal permanent damage to a properly designed sheet is observed during formation and erasure of scars and shapes (Methods). This example illustrates that groovy metasheets encode mechanically rewritable patterns that allow stable, robust, simple and repeatable formation of 3D shapes.

The grooves play multiple roles. First, they endow a metasheet with unusual soft deformations that have proven useful for the morphing of aircraft skins[25]. Stretching and bending along the groove direction ν necessitate material stretching and are thus stiff (Fig. 2a), whereas stretching and bending along the perpendicular direction ξ only require material bending and are thus soft (Fig. 2b). This allows soft metasheet deformations to be modelled as ruled surfaces[26] (Methods). Consistent with this, grooved sheets enable soft splay and twist deformations that are not accessible in flat sheets (Fig. 2c). The grooves thus enlarge the space of attainable shapes. Second, the grooves facilitate the formation of defects. Appropriate forcing, such as denting, creates defects similar to those in cylindrical shells or tape-springs[16,27–29]. These defects produce an 'H'-shaped mean curvature pattern[30] (Fig. 2d) and denting from opposite sides of the sheet yields defects with positive or negative curvature. Defects introduce geometrical frustration and store energy: their local stretching along ξ, sharp bending along ν and a dent along z

[1]AMOLF, Amsterdam, the Netherlands. [2]Huygens-Kamerlingh Onnes Laboratory, Universiteit Leiden, Leiden, the Netherlands. [3]School of Engineering and Applied Sciences, Harvard University, Cambridge, MA, USA. ✉e-mail: a.meeussen@gmail.com

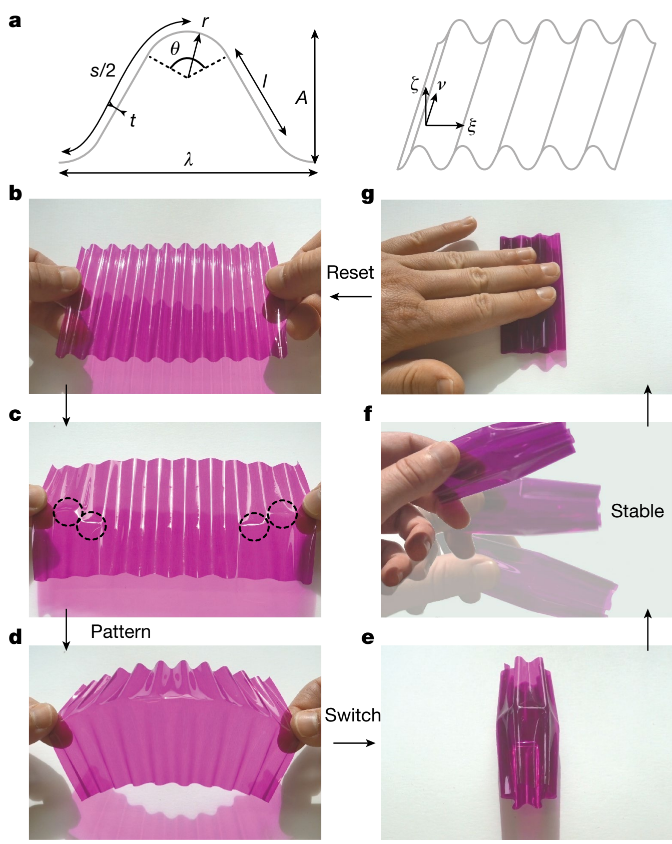

Fig. 1 | Two-step shape-morphing in groovy metasheets. a, Left: side view of undeformed groove geometry with wavelength λ, amplitude A, arc length s, thickness t, including a curved section of radius r and angle θ and a flat section of length l. Right: groovy sheet schematic showing local coordinate frame (ξ, ν, ζ). **b**, A groovy sheet, thermoformed from 40-µm-thick polyethylene terephthalate (PET) plastic (Methods). **c**,**d**, First, stretching by point forcing (**c**) along ξ leads to nucleation of defects (dashed circles), which organize in a scar (**d**). **e**–**g**, Second, after release, the scar forces the sheet to switch to a rolled state (**e**) that is stable (**f**) yet erasable (**g**).

require material stretching, as evidenced by sharp peaks in the Gaussian curvature (Fig. 2d; Methods). Crucially, the formation of defects is hysteretic, and defects can be erased by flattening the grooves via, for example, stretching. Therefore, grooves allow storage of elastic energy and memories of external forcing. Third, sheet distortions governed by the grooves facilitate the binding of defects into stable scars (Fig. 2e and Supplementary Video 1), which we demonstrate by generating two adjacent defects and dragging one along its groove. Well-separated defects are weakly pinned and easily moved (Fig. 2e(i)). When the defects are subsequently brought closer, repulsive interactions cause the mobile defect to spontaneously glide back (Fig. 2e(ii)). However, when the defects are brought very close, they attract and bind into an aligned configuration (Fig. 2e(iii)). This attraction is associated with a lowering of the elastic energy, as confirmed by simulations (Methods). Interactions between non-adjacent defects are weak (Methods and Supplementary Video 1). Attraction between adjacent defects thus produces robust stable scars, which, in analogy with origami, we refer to as mountains (+) and valleys (−). By contrast to discrete pop-through defects that can be used to shape periodically patterned sheets[12,31–33] and corrugated tubes[24], our strategy does not require one-by-one creation of individual defects and allows for scars whose location and orientation can be continuously controlled by simple manipulations. Hence, the grooves facilitate easy writing and erasure of scar patterns.

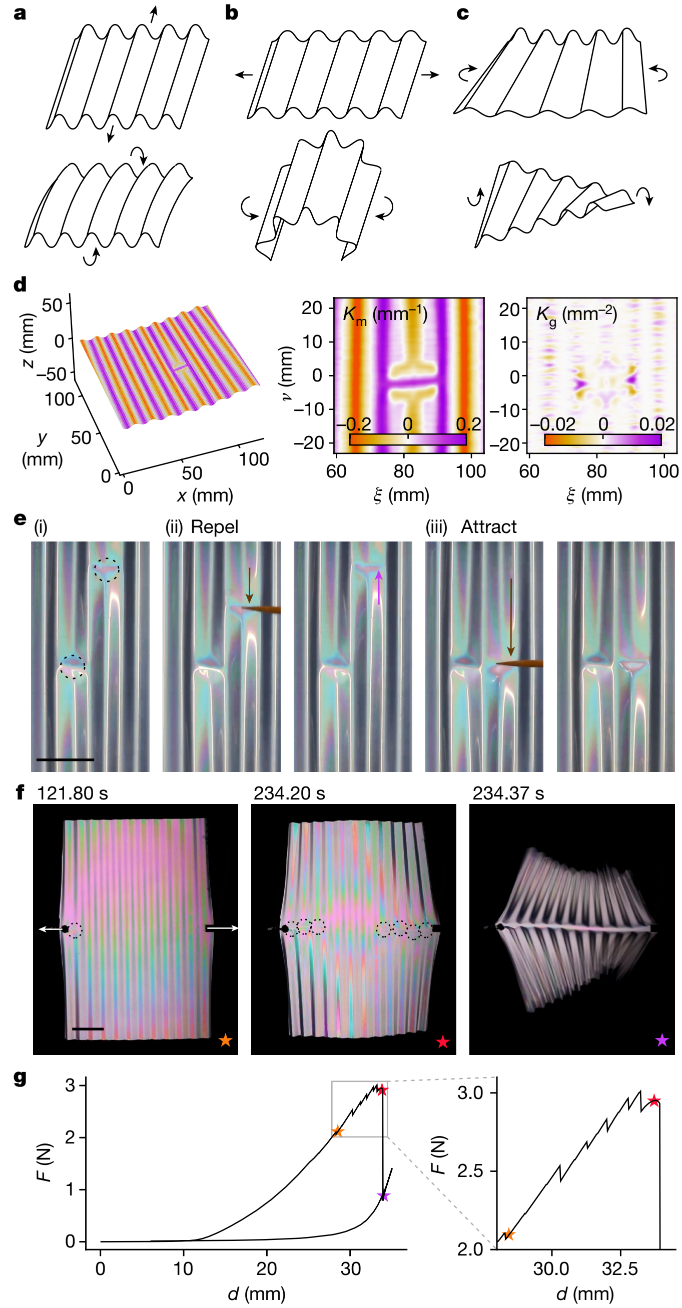

Fig. 2 | Groovy sheet geometry causes unusual mechanics. a–**c**, Undulations produce deformations that are very stiff (**a**), very soft (**b**) and of intermediate stiffness (**c**). The deformations in **b** and **c** can be approximated as ruled surfaces. **d**, Left: 3D scan of a sheet with a bistable defect (Methods), which causes a local kink but no significant overall deformation. Shading corresponds to mean curvature. Right: mean (K_m) and Gaussian (K_g) curvature near the defect. **e**, Adjacent defects ((i), dashed circles) glide along grooves under local forcing (brown arrows) or spontaneous motion (pink arrows). Defects exhibit medium-range repulsion (ii) and short-range attraction (iii), allowing defects to align into scars. **f**, Snapshots of scar formation. Defects (dashed circles) propagate stepwise from the forcing points (white arrows) until an avalanche yields a contiguous scar. Time stamps are shown. **g**, Force F versus extension d during scar formation; snapshots in **f** are indicated by coloured stars. Stretching the sheet continuously increases the force, interrupted by minor drops when defects form (enlargement, right). Abrupt scar creation results in a major force drop and transition to a second stable state. Scale bars, 2 cm.

As shown in Figs. 1 and 2f, the defects that form a scar initially propagate from the forcing points in discrete steps, after which the rest of scar forms nearly instantaneously. This observation raises important questions about the underlying mechanisms of scar formation. We can capture its phenomenology qualitatively based on two assumptions consistent with our experimental observations (Fig. 2f,g; Methods). First, defects are bistable structures that switch from a high-stress, smoothly curved configuration to a low-stress defect configuration. Second, defect formation requires local stretching along the soft direction ξ and is promoted by bending along the stiff groove direction ν. Thus, globally, defects form most easily near the edges where point forces are applied along ξ; and locally, defects—which bend the grooves along ν—facilitate the formation of neighbouring defects. In this picture, defects are first created one by one near the forcing location, as stress heterogeneity throughout the sheet is strong and cooperative effects are weak. Once multiple defects have been formed, stress heterogeneity weakens—requiring larger overall stresses to initiate defect formation—and cooperative effects become stronger. This eventually leads to an avalanche where the remaining part of the scar forms essentially instantaneously. Hence, we suggest that the propagation of defects follows from a subtle balance between cooperative and anticooperative effects (Methods).

Scars encode local stretching of the metasheet to yield complex yet controlled shapes. Consider a roll consisting of a scarred region flanked by two unscarred wings (Fig. 3a). Each defect locally flattens the metasheet yielding unidirectional extension along the scar. The wings accommodate this extension via soft splay and stretch deformations and the formation of a kink near the scar, yet relax near the sheet's edge (Fig. 3a, inset). A single groove in the scarred metasheet forms two isosceles trapezoids—isolated snapped grooves form similar shapes—and tiling these yields a roll with a circular scar (Fig. 3b). A spring-based model shows the same phenomena (Fig. 3c; Methods). Hence, we can describe scarred metasheets as stitched ruled surfaces, where patches of ruled surfaces are stitched together by stretched scars (Methods). This geometrical picture also captures our observation that the roll curvature diminishes for increased wingspan (Methods). Hence, the combination of scar stretching and flexural properties drives shape-morphing in groovy metasheets.

Using multiple scars produces complex shapes that are accurately described as stitched ruled surfaces (Fig. 3d,e; Methods). First, we note that two scars of opposite sign cannot form a roll, owing to geometric incompatibility, and instead form a helical structure (Fig. 3d). The surface in between the scars exhibits significant twist, reflecting the anomalous soft deformations of our metasheets. Second, two adjacent scars of equal sign form a dual rolled structure (Fig. 3e). Here, too, we observe twisting of the surface that connects the scars—this can be understood intuitively by noting that the metasheet is stretched along ξ by both scars which can be relaxed by twisting. A precise understanding of this emergence of twist can be obtained by modelling the relative energy penalties of sheet deformations (bend, stretch, splay and twist) and scar bending (Supplementary Information). Such models also correctly capture our observations that a single-scarred roll exhibits a bifurcation from a non-twisted state for short wings, to a twisted state for long wings (Fig. 3f; Methods).

To extend the space of achievable shapes, we relax our tacit assumptions that scars span the full sheet, that scarred sheets have no self-contacts, and that scar and grooves are perpendicular (Fig. 4a–d). First, scars with alternating positive and negative sign can be chained, yielding ribbons with arbitrary curvature sign alternations such as an '∞'-shape (Fig. 4a). Similarly, scars may be robustly terminated mid-sheet by using small perforations that function as local edges, allowing juxtaposition of curved and non-curved regions (Fig. 4b). Second, long sheet strips with a central scar may self-block during the rolling process via steric interactions, producing pretzel-like shapes (Fig. 4c).

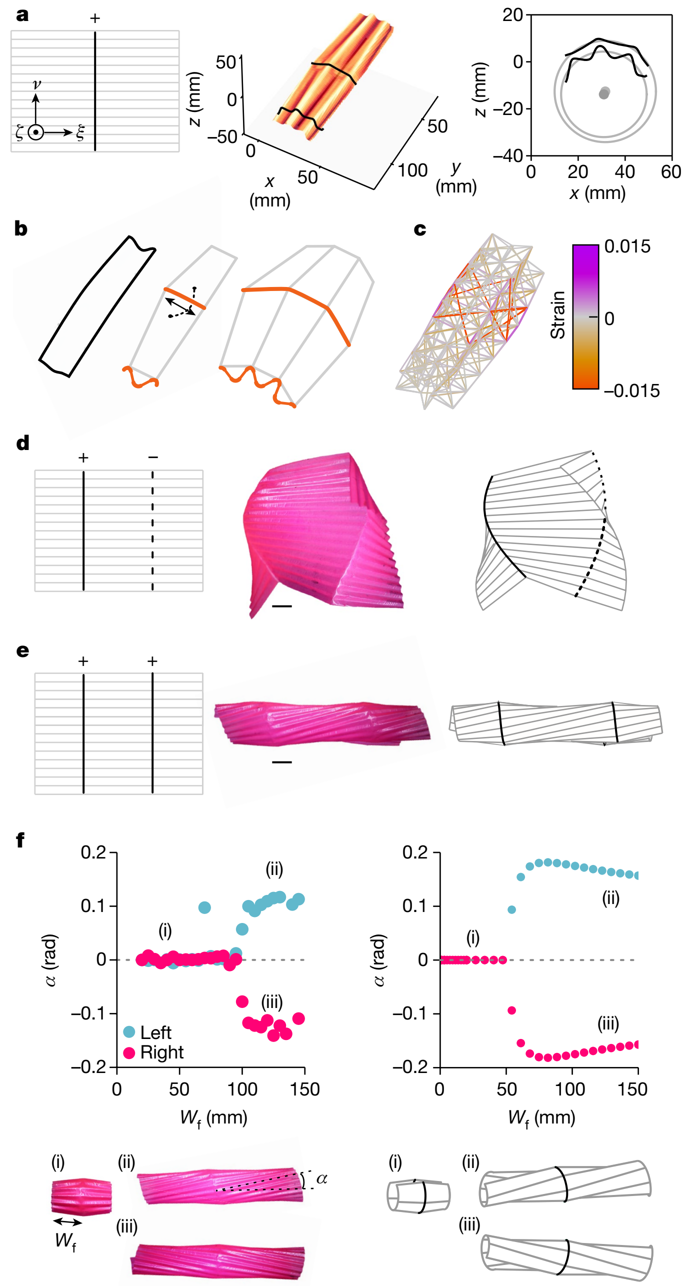

Fig. 3 | Scarred sheets yield complex yet controlled shapes. a, 3D-scanned subsection of a single-scarred (schematic, left), rolled 75-μm-thick PET plastic groovy metasheet. Colours indicate mean curvature as a guide to the eye. Right: sheet sections at the scar and near the edge (black lines) and their best-fit circles (grey lines). **b**, A single groove with a defect (left) and a sketch of its footprint (middle). Tiling scarred grooves without additional deformation yields a roll (right). **c**, A coupled-spring model exhibits the same phenomenology, and illustrates how local strain (colours) is distributed. **d**, Opposite-parity scars (left) produce helicoidal geometries (middle, scale bar, 2 cm) that are well approximated by geometric stitched ruled surfaces (right). **e**, Scars of equal parity yield rolled and twisted shapes. **f**, Experimental twist bifurcation in angle α at large size W_f of a single-scarred sheet (left) is reproduced by including deformation energy penalties in the ruled-surface model (right). For details, see Methods.

Lastly, strips with grooves and a central scar that are not orthogonal form corkscrews; allowing self-blocking yields characteristic helical perversions (Fig. 4d). Combining chaining, terminating, steric interactions and scar angles yields a wide variety of shapes. Groovy sheet

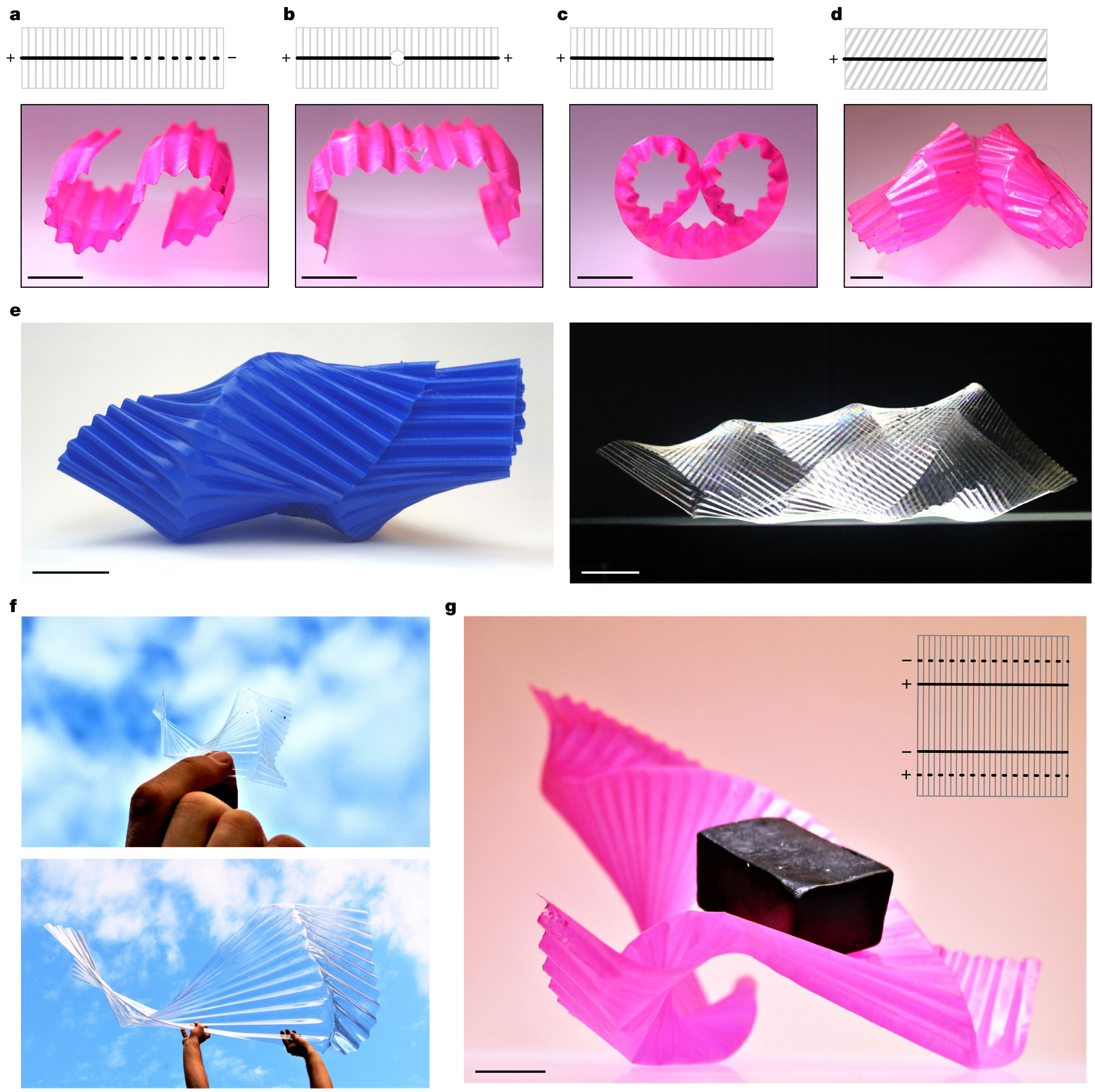

Fig. 4 | Pluripotent shape-morphing in diverse scarred groovy metasheets. **a**, Two scars, adjoined but of opposite sign (top, schematic), yield S-shaped sheets of alternating curvature (bottom). **b**, Holes allow scars to terminate midsheet, resulting in interstitial flat sections. **c**,**d**, Steric hindrance leads to pretzel rolls (**c**) or helical perversions when scar and grooves are non-parallel (**d**). Sheets in **a**–**d** are cut from commercial corrugated PET film ($t = 15\,\mu$m, $A = 1$ mm, $\lambda = 3.7$ mm) with silicone rubber spray coating of $20 \pm 10\,\mu$m for visualization. Scale bars, 1 cm. **e**, Shape-morphing is material independent: 3D-printed flexible polyester (left) and commercial corrugated PET film (right) show similar stability and shape. Scale bars, 5 cm. **f**, Sheets reshape across scales: commercial corrugated PET film (top) and PE roofing (bottom) differ in size by nearly two orders of magnitude ($\lambda = 5$ mm and 100 mm), but show similar helical shapes (compare with Fig. 3d). **g**, Multiple opposing scars (schematic shown in inset) lead to rigid curved structures: a 2.9 g sheet ($t = 23\,\mu$m, $A = 2$ mm, $\lambda = 6.4$ mm), which normally buckles under gravity, now supports ten times its own weight (black oblong, 32.3 g). Scale bar, 2 cm.

shape-morphing is realizable in a range of materials (Fig. 4e) as well as across a range of scales (Fig. 4f). In addition, scars endow groove sheets with load-bearing capabilities (Fig. 4f).

Our multistability-based strategy for robust, stable and repeatable shape-morphing is scale-free and can be extended using, for example, non-parallel undulations. We anticipate that combinations of multistable, reversible and irreversible strategies will bring metasheets with unprecedented switching, actuation and morphing capabilities within reach, with applications in sensing and actuation, prosthetics and wearables, design, (soft) robotics, self-learning materials and mechanical information processing.

Online content

Any methods, additional references, Nature Portfolio reporting summaries, source data, extended data, supplementary information, acknowledgements, peer review information; details of author contributions and competing interests; and statements of data and code availability are available at https://doi.org/10.1038/s41586-023-06353-5.

1. Sharon, E., Roman, B., Marder, M., Shin, G. S. & Swinney, H. L. Buckling cascades in free sheets. *Nature* **419**, 579 (2002).
2. Tallinen, T. et al. On the growth and form of cortical convolutions. *Nat. Phys.* **12**, 588–593 (2016).

3. Shyer, A. E. et al. Villification: how the gut gets its villi. *Science* **342**, 212–218 (2013).
4. Li, B., Cao, Y.-P., Feng, X.-Q. & Gao, H. Mechanics of morphological instabilities and surface wrinkling in soft materials: a review. *Soft Matter* **8**, 5728 (2012).
5. Klein, Y., Efrati, E. & Sharon, E. Shaping of elastic sheets by prescription of non-Euclidean metrics. *Science* **315**, 1116–1120 (2007).
6. Liu, Y., Boyles, J. K., Genzer, J. & Dickey, M. D. Self-folding of polymer sheets using local light absorption. *Soft Matter* **8**, 1764–1769 (2012).
7. Kim, J., Hanna, J. A., Byun, M., Santangelo, C. D. & Hayward, R. C. Designing responsive buckled surfaces by halftone gel lithography. *Science* **335**, 1201–1205 (2012).
8. Wu, Z. L. et al. Three-dimensional shape transformations of hydrogel sheets induced by small-scale modulation of internal stresses. *Nat. Commun.* **4**, 1586 (2013).
9. Gelebart, A. H. et al. Making waves in a photoactive polymer film. *Nature* **546**, 632–636 (2017).
10. Siéfert, E., Reyssat, E., Bico, J. & Roman, B. Programming curvilinear paths of flat inflatables. *Proc. Natl. Acad. Sci. USA* **116**, 16692–16696 (2019).
11. Guseinov, R., McMahan, C., Pérez, J., Daraio, C. & Bickel, B. Programming temporal morphing of self-actuated shells. *Nat. Commun.* **11**, 237 (2020).
12. Silverberg, J. L. et al. Using origami design principles to fold reprogrammable mechanical metamaterials. *Science* **345**, 647–650 (2014).
13. Celli, P. et al. Shape-morphing architected sheets with non-periodic cut patterns. *Soft Matter* **14**, 9744–9749 (2018).
14. Rafsanjani, A. & Bertoldi, K. Buckling-induced kirigami. *Phys. Rev. Lett.* **118**, 084301 (2017).
15. Dieleman, P., Vasmel, N., Waitukaitis, S. & van Hecke, M. Jigsaw puzzle design of pluripotent origami. *Nat. Phys.* **16**, 63–68 (2020).
16. Jules, T., Lechenault, F. & Adda-Bedia, M. Curving origami with mechanical frustration. *Extrem. Mech. Lett.* **46**, 101315 (2021).
17. Yan, Z. et al. Controlled mechanical buckling for origami-inspired construction of 3D microstructures in advanced materials. *Adv. Funct. Mater.* **26**, 2629–2639 (2016).
18. Rafsanjani, A., Zhang, Y., Liu, B., Rubinstein, S. M. & Bertoldi, K. Kirigami skins make a simple soft actuator crawl. *Sci. Robot.* **3**, eaar7555 (2018).
19. Rus, D. & Tolley, M. T. Design, fabrication and control of origami robots. *Nat. Rev. Mater.* **3**, 101–112 (2018).
20. Miskin, M. Z. et al. Electronically integrated, mass-manufactured, microscopic robots. *Nature* **584**, 557–561 (2020).
21. Liu, Q. et al. Micrometer-sized electrically programmable shape-memory actuators for low-power microrobotics. *Sci. Robot.* **6**, eabe6663 (2021).
22. Liu, K., Hacker, F. & Daraio, C. Robotic surfaces with reversible, spatiotemporal control for shape morphing and object manipulation. *Sci. Robot.* **6**, eabf5116 (2021).
23. Norman, A. D., Seffen, K. A. & Guest, S. D. Multistable corrugated shells. *Proc. R. Soc. A Math. Phys. Eng. Sci.* **464**, 1653–1672 (2008).
24. Bende, N. P. et al. Overcurvature induced multistability of linked conical frusta: how a 'bendy straw' holds its shape. *Soft Matter* **14**, 8636–8642 (2018).
25. Dayyani, I., Shaw, A. D., Saavedra Flores, E. I. & Friswell, M. I. The mechanics of composite corrugated structures: a review with applications in morphing aircraft. *Compos. Struct.* **133**, 358–380 (2015).
26. Audoly, B. & Pomeau, Y. *Elasticity and Geometry* (Oxford Univ. Press, 2010).
27. Walker, M. G. & Seffen, K. A. On the shape of bistable creased strips. *Thin-Walled Struct.* **124**, 538–545 (2018).
28. Seffen, K. A., Wang, B. & Guest, S. D. Folded orthotropic tape-springs. *J. Mech. Phys. Solids* **123**, 138–148 (2019).
29. Boudaoud, A., Patrício, P., Couder, Y. & Ben Amar, M. Dynamics of singularities in a constrained elastic plate. *Nature* **407**, 718–720 (2000).
30. Wildeman, S. Real-time quantitative Schlieren imaging by fast Fourier demodulation of a checkered backdrop. *Exp. Fluids* **59**, 97 (2018).
31. Oppenheimer, N. & Witten, T. A. Shapeable sheet without plastic deformation. *Phys. Rev. E* **92**, 052401 (2015).
32. Plummer, A. & Nelson, D. R. Buckling and metastability in membranes with dilation arrays. *Phys. Rev. E* **102**, 33002 (2020).
33. Faber, J. A., Udani, J. P., Riley, K. S., Studart, A. R. & Arrieta, A. F. Dome-patterned metamaterial sheets. *Adv. Sci.* **7**, 2001955 (2020).

Methods

Sheet fabrication and shape

We thermoform biaxially oriented polyethylene terephthalate sheets (Dupont Teijin Mylar-A) to obtain reproducable corrugated geometries (Extended Data Fig. 1). The 25–100-µm-thick PET films are placed on a 30-by-30 cm aluminium sheet with machined grooves. Screw-in inserts are used to push the film into each corrugation (Extended Data Fig. 1a). The assembly is heated to 120 °C for approximately 1.5 h in a commercial oven, followed by around an at least 2 h cooling period before removal of the formed sheet. The mould's geometry is set by amplitude $A = 6.8$ mm, wavelength $\lambda = 7.4$ mm, mean radius of curvature $R = 1.5$ mm, groove angle $\theta = 160°$, facet length $l = 4.4$ mm and insert spacing $d = 50$ µm (Extended Data Fig. 1b). A typical resulting groove shape for 75-µm-thick film is illustrated in Extended Data Fig. 1c,d, showing a good match between mould and sheet shape.

Elastic and plastic deformations

We investigate under which conditions our sheets behave elastically, and show that defects do not lead to appreciable plastic deformation of groovy sheets. Shape-morphed groovy sheets exhibit defects analogous to those found in snapped tape-spring measures. Previous work has shown that the maximal change of curvature across the snapped region is approximately equal to the tape's initial curvature[28]. On the basis of this finding, we estimate the maximal strain induced by a defect in a groovy sheet as $\epsilon_{\max} = \frac{tR}{2}$. Assuming an elastic-plastic material model $\sigma = E\epsilon$ in which $\epsilon < \epsilon_y$, $\sigma = E\epsilon_y = \sigma_y$: $\epsilon > \epsilon_y$, the no-yield condition is then given by $R > \frac{t}{2\epsilon_y} = \frac{t}{2}\frac{E}{\sigma_y}$.

Fracture testing following ASTM-D882 on three Mylar-A samples using an Instron 3360 universal testing machine and Instron 2530 100 N static load cell produce an average yield strain of $\epsilon_y = 0.025 \pm 0.007$. Sheets of thickness $t = [25, 50, 75, 100]$ µm used in this work thus require groove radius of curvature $R > [0.5, 1, 1.5, 2]$ mm to ensure elastic behaviour. Sheets used throughout this paper lie above this boundary and, consistent with this fact, we observe no appreciable plastic deformation, indicating that elasticity rather than plasticity governs shape-morphing in groovy sheets.

We emphasize that the above rule of thumb is material agnostic. For example, for metal sheeting, a typical Young's modulus $E = \mathcal{O}(100)$ GPa and yield stress $\sigma_y = \mathcal{O}(0.1)$ GPa result in $R > 500t$; at a typical thickness $t = 0.5$ mm, groove radius designs above $R \approx 25$ cm should result in groovy sheets with elastic reshaping behaviour.

Defect formation energy

We measure the formation energy of a single defect in a 75-µm-thick groovy sheet of $W = 100 \pm 5$ mm length (Extended Data Fig. 2).

We use a horizontal Instron 4900-series universal testing machine outfitted with an Instron 2530 10 N load cell. The sample is placed on two stiff supports $w = 50$ mm apart and probed with an indenter secured to the sample with a ball magnet (Extended Data Fig. 2a). The indenter is displaced by u at 0.1 mm s^{-1}, resulting in popping of the groove while forces F are measured. Extended Data Fig. 2b shows resulting data for popping (upper curve) and unpopping (lower curve, obtained by indenting a reversed defected sample) of a sheet with $N = 5$ grooves. Calculation of the area under the curve yields an experimental estimate of popping and unpopping energies of 1.7 mN m and 0.1 mN m, respectively.

Extended Data Fig. 2c shows collected popping data for $N \in [0.5, 1, 2, 3, 5]$ grooves. The defect at $N = 0.5$ is not stable. Two characteristic snapping events are observed for $N \in [1, 2, 3, 5]$ (grey areas). The resulting areas under each curve yield popping energy estimates that increase with N and appear to reach a plateau value at $N = 5$ (Extended Data Fig. 2d), indicating that defects' elastic interaction range is limited to several grooves.

3D imaging

3D images of groovy sheets are obtained using fringe-projection imaging[30] (Extended Data Fig. 3). An Epson EMP-X3 projector sequentially images a sinusoidal fringe pattern with distinct phase offsets $\Delta\psi \in [0, \pi/2, \pi, 3\pi/2]$ on a reference surface at $l_1 = 110$ cm distance. A Basler acA2040-25gm camera with Kowa 75 cm focus lens at $l_2 = 15$ cm from the projector records the fringe images at wavelength $\lambda = 52.7$ px, yielding a spatial resolution of 0.075 mm px^{-1} (Extended Data Fig. 3a). When an object is placed in front of the reference surface, the projected fringe pattern is distorted (Extended Data Fig. 3b); the phase difference $\Delta\phi$ between reference and distorted images yields an estimate of the sample's height profile Δz via

$$
\begin{aligned}
|\mathbf{p}_a - \mathbf{p}_c| &= \frac{\lambda}{2\pi}\Delta\phi \\
\Delta z = |\mathbf{p}_d - \mathbf{p}_b| &= \frac{|\mathbf{p}_a - \mathbf{p}_c| l_1}{|\mathbf{p}_a - \mathbf{p}_c| + l_2},
\end{aligned}
\tag{1}
$$

with $\mathbf{p}_a$, $\mathbf{p}_b$, $\mathbf{p}_c$ and $\mathbf{p}_d$ as shown in Extended Data Fig. 3a. Height profile noise, due to the projector's resolution and deviation of the fringes from pure sinusoids, is filtered via two-dimensional Gaussian smoothing over 0.75 mm and one-dimensional Gaussian smoothing over 2 mm orthogonal to the fringes (Extended Data Fig. 3c), yielding typical height profiles such as that shown in Extended Data Fig. 3d.

Computational spring model

We present a simple numerical spring model that approximates a groovy sheet's geometry and stiffness. More precise homogenized models[25] may be used in future work. However, the spring model exhibits the same qualitative behaviour as real sheets, showing that reshaping is robust and can be captured by elastic, geometry-governed deformations.

The model, shown in Extended Data Fig. 4a, is built from squares of Hookean springs (length $l = 1$, stiffness $k_s = 1$) cross-braced by diagonal springs ($k_{sd} = 0.1k_s$), placed in an accordion pattern at fold angle $\phi^0 = 2.1$ rad and connected by N_x-by-N_y nodes (linear torsional stiffness $k_t = 10^{-4}l^2k_s$). The resulting structure qualitatively mimics a $l(N_y - 1)$-by-$l(N_x - 1)\cos\frac{\phi^0}{2}$ groovy sheet (Extended Data Fig. 4b).

Generally, we may approximate the model's minimal-energy configuration (encoded by node positions $\mathbf{Q}$ at time t) under an applied node displacement via a gradient descent algorithm:

$$
\mathbf{Q}^{t+1} = \mathbf{Q}^t - \alpha\nabla_Q\mathcal{E}(\mathbf{Q}^t), \tag{2}
$$

where $\mathcal{E}$ is the system's elastic energy and $\alpha = 0.25$ the descent speed. To limit computational complexity, we choose $t_{\max} = 10^6$ iterations per optimization step.

In particular, the shape-morphed sheet in Fig. 1e is obtained from this spring model, starting from a configuration at rest, displacing two opposing boundary nodes over six steps until they are separated by the flattened sheet length, and finally allowing the structure to relax freely over 14 steps, resulting in a well-converged solution with minimal geometric change ($|\Delta\mathbf{Q}| < 10^{-6}$).

Defect interactions in experiment and numerics

Defects in a groovy sheet interact via geometry-mediated elastic interactions. Experiments on a 50-µm-thick sample, shown in Supplementary Video 1, indicate that defects separated by one or more grooves do not interact significantly, whereas adjacent defects interact strongly and dominate the sheet's reshaping behaviour. Specifically, defects of equal sign in adjacent grooves exhibit short-range attraction and long-range repulsion. Here, we briefly discuss experimental and numerical evidence for these interactions.

First, sheet deformations may be decomposed into mean and Gaussian curvature K_m and K_g, associated with material bending and stretching. The curvatures are obtained from 3D-scanned height profiles $z(x, y)$ via[26]:

$$K_{\mathrm{m}}=\frac{1}{2\left(1+\frac{\partial z}{\partial x}^{2}+\frac{\partial z}{\partial y}^{2}\right)^{3/2}}\left(\left(1+\left(\frac{\partial z}{\partial x}\right)^{2}\right)\frac{\partial^{2}z}{\partial y^{2}}+\left(1+\left(\frac{\partial z}{\partial y}\right)^{2}\right)\frac{\partial^{2}z}{\partial x^{2}}-2\frac{\partial z}{\partial x}\frac{\partial z}{\partial y}\frac{\partial z}{\partial x\partial y}\frac{\partial z}{\partial y\partial x}\right) \quad (3)$$

$$K_{\mathrm{g}}=\frac{\frac{\partial^{2}z}{\partial x^{2}}\frac{\partial^{2}z}{\partial y^{2}}-\frac{\partial z}{\partial x\partial y}\frac{\partial z}{\partial y\partial x}}{\left(1+\frac{\partial z}{\partial x}^{2}+\frac{\partial z}{\partial y}^{2}\right)^{2}},$$

where $\frac{\partial z}{\partial x}$ is approximated by the five-point discrete derivative at each grid site (x_i, y_i):

$$\left.\frac{\partial z}{\partial x}\right|_{x_i,y_i}\approx\frac{8(z(x_{i+1},y_i)-z(x_{i-1},y_i))-(z(x_{i+2},y_i)-z(x_{i-2},y_i))}{6(x_{i+1}-x_{i-1})} \quad (4)$$

The above equations were used to obtain the curvatures of the 75-µm-thick thermoformed BoPET sheet shown in Fig. 2d. Extended Data Fig. 5 shows curvature distributions for adjacent defects at variable spacing.

Each defect, placed at a groove crest, yields a characteristic pattern of Gaussian curvature (K_g) in adjacent troughs (Extended Data Fig. 5a,b). Well-separated defects in adjacent crests feature two such patterns in their shared trough. When brought close together, the patterns merge into a 'diamond' pattern of lower magnitude (Extended Data Fig. 5c). We hypothesize that the weaker Gaussian pattern for bound defects corresponds to a reduction in stretching energy.

The reduction of energy for adjacent defects is supported by numerical calculations in the spring model (see above) on two grooves ($N_x = 5$, $N_y = 21$) with two defects at variable spacing d (Extended Data Fig. 5d). The model's total elastic energy $\mathcal{E}$ is a measure of defect interaction strength (Extended Data Fig. 5e) and shows a small reduction for bound defects at $d = 0$, indicating close-range attraction.

Scar formation

We describe how scars form under point loading of a groovy sheet in both experiments and simulations, and propose a theoretical model that reproduces key features of the phenomenon.

Experiment. As shown in Extended Data Fig. 6a, a groovy sheet is attached at two edge points to an Instron 3360 universal testing machine fitted with an Instron 2530 10 N static load cell. The sample is extended by a distance d as shown by the profile in Extended Data Fig. 6b. The force F is recorded, as well as a video of the sample. Initially, sequential snapping events near the loading points lead to minor force drops; finally, an avalanche where the remaining part of the scar forms at high speed leads to a major force drop (Fig. 2f,g and Extended Data Fig. 6c). Snapping events are automatically identified from video footage by comparing differences between consecutive images (Extended Data Fig. 6c, orange line) in a region near the scar (Extended Data Fig. 6a, dashed box); large differences correspond to snapping events (Extended Data Fig. 6c, dashed grey lines).

Simulation. A computational model (Methods) is used to simulate a sheet similar to the experimental sample above (Extended Data Fig. 6d). The simulated sheet is placed under stepwise point loading at opposing edge nodes and elongated by a distance d over 1,000 simulation steps. The resulting force F is recorded and shown in Extended Data Fig. 6e. Minor force drops corresponding to one-by-one defect formation are observed, as is a rapid major force drop when the full scar is formed (Extended Data Fig. 6f). Convergence of the static model during dynamic snap-through events—measured by geometric change $|\Delta\mathbf{Q}|$ of the sheet's node positions $\mathbf{Q}$—is fair ($|\Delta\mathbf{Q}| < 10^{-3}$). The qualitative similarity of experiment and simulation shows that scar formation is a robust phenomenon.

Theory. We now introduce a simple theoretical model that aims to capture three experimental observations: (1) initially, defects appear one at a time; (2) defects nucleate near the edges and then propagate inwards contiguously; (3) after enough defects have appeared, the full scar is formed during a sudden avalanche.

To capture (1), we model the state of each groove i (with or without defect) by a binary state variable s_i (0 or 1, respectively). To represent the transition between the two states, we assume a bilinear relation between force f_i and extension d_i (Extended Data Fig. 6g): the undefected state with unity stiffness switches—via a force drop at a critical force f_i^{c}—to the defected state with larger stiffness. A small random offset is added to each unit's critical force to prevent degeneracies. As the grooves are coupled in series, the overall force F is equal to the force f_i on each unit. As in the experiment above, we drive a chain of $n = 12$ bistable units by applying an increasing global extension $d = \sum_i^n d_i$. Initially, all units are in state 0. For given d and chain state configuration $\mathbf{S} \coloneqq (s_1, \ldots s_i, \ldots)$, d_i and F can be calculated implicitly; whenever $F > f_i^{\mathrm{c}}$ for a unit in state $s_i = 0$, its state is switched to $s_i = 1$, and d_i and F are recalculated. This model gives rise to one-by-one state switching of each unit, analogous to defect formation in a groovy sheet. Specifically, whenever a unit switches to state 1, the global force F drops and the remaining units relax. Hence, observation (1) follows from the combination of serially coupled grooves and force balance; however, the sequence of state switches is set by the noise on f_i^{c}, and there are no avalanches.

We now capture observations (2) and (3) by adding inhomogeneities and interactions to the model. As the main text argues, defects form in a scar formation owing to three effects: global stretching (as in the model above); high stress near the forcing location (inhomogeneity); and bending induced by neighbouring defects (interactions).

We first add inhomogeneity, which can be represented as a stress that decays away from the forcing point. We model this through each unit's critical force: $f_i^{\mathrm{c}} = f^{\mathrm{c}(0)} + \lambda\sin(\pi i/(2n))$, so that critical forces increase further into the bulk. Although we set $f^{\mathrm{c}(0)} = 1$, $\lambda = 0.1$ here, note that our results are sensitive to neither the precise values nor the spatial decay profile of f_i^{c}. Second, we add interactions. Defect formation in a unit (transition from state 0 to 1) is promoted if neighbouring units sport defects (are in state 1). Moreover, although a single defect hardly bends the sheet (Fig. 2d), a chain of several defects leads to appreciable bending (Fig. 2f). To model this effect, we lower the critical force of units that are directly adjacent to a patch of l defects by an amount $\Delta f_i^{\mathrm{c}} = -c\, l^p$. With inhomogeneity and interactions included in our model, we find that a broad range of heterogeneity strengths (λ) and interaction parameters (c, p) lead to defects nucleating from the forcing points as well as contiguous defect formation, explaining observation (2). Finally, to capture observation (3)—emergence of an avalanche—nonlinear defect cooperativity ($p = 2$) appears to be necessary. All in all, defect formation in the bulk is thus suppressed by inhomogeneity, yet encouraged by interactions.

We find that the combination of these two competing effects leads to runaway defect formation—that is, scarring— at a critical value of overall stretching and scar length. Even though a full study of this heuristic model (as well as connecting it to the physics of thin sheets) is beyond this study, we find that a surprisingly wide variety of parameters produces realistic results (Extended Data Fig. 6h), underlining the robustness of scar formation.

Experimental scarred sheet shapes

We describe the experimental shaping effect of scar lines placed symmetrically in a groovy sheet, orthogonal to the grooves. A single scar line produces rolls, two equal-parity scar lines produce twisted cylinders and two opposite-parity scar lines result in helicoids (Extended Data Fig. 7).

Extended Data Fig. 7a shows the shaping effect of a single scar line, placed centrally in a sheet of variable width $2W_f$. Local stretching and curving of the scar cause the sheet to roll into a cylinder with radius of curvature R_s at the scar. R_s initially grows with increasing sheet width, but saturates to a constant value. We believe this saturation emerges because of a weak bending of the grooves, which may lower elastic energy at larger sheet widths. In addition, at intermediate sheet width, a sharp transition from no twisting to finite twisting is observed in angle α between the grooves and rolling axis. Symmetric left- and right-twisting states are seen.

Sheets with two equal-parity scar lines are studied for varying scar–scar distance D and scar–edge distance W_f (Extended Data Fig. 7b). All observed shapes roll into a cylindrical shape, described by the central radius of curvature R_c, with an additional persistent twist described by angle α between the grooves and rolling axis. The sheets' spontaneous twisting can be understood intuitively by envisioning two single-scarred sheets that must be joined to create a double-scarred sheets. Attaching two rolled sheets as is necessitates groove bending at high stretching energy cost; however, this geometric frustration can be relieved by low-energy twisting deformations. Symmetric left- and right-twisting states are observed and shown in Extended Data Fig. 7b. The sheet's rolling radius depends weakly on sheet size; conversely, the twisting angle decreases with growing scar–scar distance.

Two opposite-parity scar lines result in helicoidal shapes, quantified by a twisting angle per groove β and a groove wavelength λ_c at the helicoid axis (Extended Data Fig. 7c). Both shape metrics decrease as the scar–scar distance D grows; the scar–edge distance W_f shows no significant shape impact. If the sheet shape is indeed helicoidal, a geometric relation between λ_c and β exists. Let us assume that scars are helicoids with radius of curvature $R = D/2$ and pitch $2\pi T = \frac{2\pi}{\beta}\lambda_c$. The scar arc length over the central axis section $l = \lambda_c$ is then given by $\sqrt{R^2 + T^2}\,\frac{l}{T}$. Assuming that grooves at the scar are completely flattened to the full arc length s, the axis wavelength and twist per groove are related via

$$\lambda_c = \sqrt{s^2 - \left(\frac{D}{2}\beta\right)^2}, \tag{5}$$

which compares favourably to the measured data (Extended Data Fig. 7c, right). Thus, groovy sheets with two opposite-parity scars form helicoidal surfaces to a good approximation.

Geometric ruled-surface model of sheets with one scar

Here we describe scarred sheets as ruled surfaces: the scar line forms a generating curve and grooves are modelled as straight lines that point away from this base curve. Ruled surfaces can capture the shape of a groovy sheet undergoing soft deformations (Fig. 2a). Soft deformations are defined as (1) stretching and bending along ξ, which couple linearly to material bending; and (2) in-plane splay and out-of-plane twist, which couple linearly to material bending and quadratically to material stretching[26].

In our ruled-surface model, we approximate the scar line as a helical curve $\mathbf{h}(t)$ with radius R and wavelength $2\pi T$ (we denote by T the helix length), which is described by the parametrization

$$\mathbf{h}(t) = (R\cos t, R\sin t, Tt), \tag{6}$$

as shown in Extended Data Fig. 8a. The base curve has a local coordinate frame (the Serret–Frénet frame), which is given by the tangent, normal and binormal vectors:

$$\hat{\mathbf{t}} = \frac{1}{\sqrt{R^2 + T^2}}(-R\sin t, R\cos t, T) \tag{7}$$

$$\hat{\mathbf{n}} = (-\cos t, -\sin t, 0) \tag{8}$$

$$\hat{\mathbf{b}} = \frac{1}{\sqrt{R^2 + T^2}}(T\sin t, -T\cos t, R). \tag{9}$$

The angle between the binormal vector and the cylinder axis is set by $\alpha = \arctan T/R$. The helix' curvature k and torsion g are constants, calculated to be $k = \left|\frac{\partial t}{\partial s}\right| = \frac{|R|}{T^2 + R^2}$ and $g = \hat{\mathbf{b}} \cdot \left|\frac{\partial n}{\partial s}\right| = \frac{T}{T^2 + R^2}$, where $s = \sqrt{T^2 + R^2}\,t$ is the arc length along the helix.

Extended Data Fig. 8b illustrates how we model grooves as straight lines $\mathbf{g}(w, t) = w\hat{\mathbf{g}} + \mathbf{h}(t)$ of length $w \in [0, W_f]$, that start at point $\mathbf{h}(t)$ at the scar line and point away from it along vectors $\hat{\mathbf{g}} = \cos\beta\hat{\mathbf{b}}(t) + \sin\beta\hat{\mathbf{n}}(t)$ with no tangential component (note that this tangential component corresponds to significant material stretching at the scar line, and we assume such stretching to be negligible because of its high energetic cost). Together, the radius R and helix length T of the scar line, and the angle β and length W_f of the grooves, completely set the 3D shape of the scarred groovy sheet.

Geometric ruled-surface model of sheets with two scars

Analogous to the ruled-surface model for single scars above, we describe a sheet section of length W_f flanked by two parallel scar lines as a ruled surface connected to two helical base curves $\mathbf{h}(t)$ and $\mathbf{c}(t)$.

We construct the two-scar surface starting from a helical scar line $\mathbf{h}(t)$, defining grooves $\mathbf{g}(W_f, t)$ as rules of length W_f pointing away from $\mathbf{h}(t)$, and connecting the groove ends by a secondary scar line $\mathbf{c}(t)$. Generically, $\mathbf{c}(t)$ can be parametrized as

$$\mathbf{c}(t) = \mathbf{h}(t) + \mathbf{g}(W_f, t) = \begin{pmatrix} C\cos(t+\phi) \\ C\sin(t+\phi) \\ Tt + W_f\cos\beta\cos\alpha \end{pmatrix}. \tag{10}$$

The secondary scar line is another helicoid with pitch pitch $2\pi T$ around the same axis as the base curve $\mathbf{h}$. Its radius is $C = \mathrm{sgn}(R - W_f\sin\beta)\sqrt{(R - W_f\sin\beta)^2 + (W_f\cos\beta\sin\alpha)^2}$, and its phase is shifted with respect to the primary scar line by the fixed angle $\phi = -\arctan\frac{W_f\cos\beta\sin\alpha}{R - W_f\sin\beta}$.

Assuming the material behaves the same at both scars $\mathbf{h}$ and $\mathbf{c}$, two adjacent rules must have the same spacing at both curves, satisfying

$$|\mathbf{h}(\Delta t) - \mathbf{h}(0)|^2 = |\mathbf{c}(\Delta t) - \mathbf{c}(0)|^2, \tag{11}$$

where Δt is a rule spacing parameter that can be related to the physical groove wavelength at the scar d^0 via $|\mathbf{h}(\Delta t) - \mathbf{h}(0)|^2 = T^2\Delta t^2 + 2(1 - \cos\Delta t)(R^2) = (d^0)^2$. The rule spacing constraint implies that $|C| = |R|$ (which greatly reduces the number of available shapes). This equality is satisfied if

$$\sin^2\beta - \frac{2(R^{*2} + T^{*2})}{R^*}\sin\beta + \frac{T^{*2}}{R^{*2}} = 0, \tag{12}$$

where $T^* = T/W_f$ and $R^* = R/W_f$. This equation describes a phase diagram of geometrically admissible shapes for a double-scarred sheet: each combination of β and T^* corresponds to a unique value of R^*. Sketches of the shapes are shown in Extended Data Fig. 9. Visual inspection shows shapes close to experimentally observed geometries sporting equal- and opposite-parity scars (solid and dashed boxes, respectively).

Energetic model for one scar

Here we describe sheets as ruled surfaces with added elasticity, which reproduces experimentally observed sheet shapes in the presence of a single central scar (Extended Data Fig. 10a). Crucially, the model qualitatively reproduces the twisting bifurcation at increased sheet width, indicating the transition is due to an energetic competition between sheet and scar deformations.

We first consider scar line elasticity. We assume that the scar line has a preferred curvature $k^0 = \frac{1}{R^0}$ and torsion $g^0 = 0$. We estimate the resting radius $R^0 \approx \frac{s_\lambda}{2\sin\theta/2} = \mathcal{O}(10\ \text{mm})$, based on the experiments illustrated in Extended Data Fig. 7a; we assume that grooves are flattened completely at the scar line to their full arc length s_λ. Deviations from k^0 and g^0 over a scar line section of length s_λ are then penalized via:

$$\mathcal{E}_k \propto (k - k^0)^2 s_\lambda, \tag{13}$$

$$\mathcal{E}_g \propto (g - g^0)^2 s_\lambda. \tag{14}$$

Second, we assume that grooves point orthogonally away from the scar line at a small preferred folding angle β^0. We estimate $\beta^0 \approx 0.2$ based on experiments (Extended Data Fig. 7a). We assume that the folding of grooves around the scar line takes place over a characteristic width comparable with the groove wavelength λ. The energy cost for deviations of the folding angle β over a scar line section of length s_λ is then modelled as

$$\mathcal{E}_\beta \propto \left(\frac{\beta - \beta^0}{\lambda}\right)^2 s_\lambda. \tag{15}$$

Third, we attribute an energy cost to sheet deformations away from the scar line. The sheet prefers to remain flat, its grooves parallel and at fixed mutual distance λ; thus, rolling, splaying (either in- or out-of-plane) and stretching of the grooves is penalized. We first consider rolling. Specifically, if the scar line has a finite radius of curvature R, the sheet's local curvature at a distance w from the scar line is given by $k(w) = \frac{R(w)}{R(w)^2 + T^2}$, where $R(w) = \sqrt{(R - w\sin\beta)^2 + (w\sin\alpha\cos\beta)^2}$. The energy cost to deviate from the flat state, $k(w) = 0$, is then given by

$$\mathcal{E}_r \propto \int_0^{W_\mathrm{f}} k(w)^2 \mathrm{d}w. \tag{16}$$

Finally, we consider groove splaying and stretching. Neighbouring grooves have a preferred constant distance λ. The actual distance $d(w)$ between neighbouring grooves, attached to a scar line with radius of curvature R and pitch $2\pi T$, is given by

$$d^2(w) = T^2t^2 - 2Rw\sin\beta + 2(1-\cos t)\left(R^2 - w^2\left(1 - \frac{R^2}{R^2+T^2}\cos^2\beta\right)\right) \tag{17}$$

where t is defined via ${s_\lambda}^2 = T^2t^2 + 2R^2(1-\cos t)$. The corresponding groove strain is then given by $\epsilon(w) = \frac{d(w) - \lambda}{\lambda}$. Assuming that groove deformations take place over distances of order λ, we define a groove strain energy

$$\mathcal{E}_s \propto \frac{1}{\lambda^2}\int_0^{W_\mathrm{f}} \epsilon(w)^2 \mathrm{d}w. \tag{18}$$

The total sheet energy is given by:

$$\mathcal{E}_\mathrm{tot} = K_\mathrm{k}\mathcal{E}_\mathrm{k} + K_\mathrm{gs}\mathcal{E}_\mathrm{gs} + K_\beta\mathcal{E}_\beta + K_\mathrm{s}\mathcal{E}_\mathrm{s} + K_\mathrm{r}\mathcal{E}_\mathrm{r}, \tag{19}$$

where $K_\mathrm{k}, K_\mathrm{gs}, K_\beta, K_\mathrm{s}, K_\mathrm{r} = \{K\}$ are the stiffnesses of the sheet against the deformations listed above (Extended Data Fig. 10a, right); stiffness K_k (scar rolling), K_gs (scar torsion), K_β (wing angle changes), K_s (sheet splay) and K_r (sheet rolling). The precise values of $\{K\}$ are difficult to determine theoretically. However, scar deformations are associated with material stretching, whereas groove deformations are governed by material bending which is significantly softer. We choose $K_\mathrm{k}, K_\mathrm{gs}, K_\beta = 1$, $K_\mathrm{s}, K_\mathrm{r} = 0.1$. The minimal-energy configuration of a sheet (given the equilibrium parameters k^0, λ, s_λ and β^0 for the scar curvature, groove wavelength, groove arc length and scar folding angle) are then found through numerical minimization of equation (19).

Modelled equilibrium shapes are illustrated in Extended Data Fig. 10b for short, intermediate and long widths. The sheet shapes match experimental observations: narrow sheets roll, whereas wide sheets also twist. Extended Data Fig. 10b shows how the rolling radius of curvature at the scar R, helix length T and groove angle α vary with the sheet width W_f. Results show qualitative agreement with experimentally observed shapes (Fig. 3f) in terms of magnitude and trend. First, the rolling radius starts around R^0 at $W_\mathrm{f} = 0$ and subsequently increases to $R^0 + \Delta R$ over the simulated range of W_f. Experiments show that the rolling radius reaches a plateau; this feature is not reproduced by our model, which we attribute to the absence of groove bending in our theory. Second, the helix length T undergoes a bifurcation at a critical sheet width W_f^*, increasing to a final value T^*. Lastly, the corresponding groove angle $\alpha = \arctan T/R$ undergoes the same bifurcation, reaching a final value α^*. Crucially, shape measures ΔR and α^* and bifurcation measure W_f^* match experimental values within a factor 2 (compare with Extended Data Fig. 7a).

Our simple model indicates that an energetic competition between deformations of the scar and sheet yields a twisting bifurcation at finite sheet width, consistent with experimental observations.

Note that a large spectrum of stiffnesses $\{K\}$ reproduces both the twisting bifurcation and the overall sheet shape. Extended Data Fig. 10c shows the shape measures ΔR, T^* and α^* as well as bifurcation measure W_f^* for variations of $K_\mathrm{k}, K_\mathrm{gs}, K_\beta, K_\mathrm{s}, K_\mathrm{r}$ in the range $[10^{-3}, 10]$. A bifurcation is observed in the studied range of W_f for nearly all stiffnesses; postbifurcation shapes with radii around 20 mm and groove angles around 0.15 rad are seen throughout, indicating that the twisting effect of scars is particularly robust against stiffness variations. We therefore expect the reshaping behaviour of scar lines in groovy sheets to be consistent across a wide range of geometries and materials.

Data availability

The data that support the findings of this study are available in the online version of this paper. Source data are provided with this paper. All other data are available on request from the corresponding author.

Code availability

The code that supports the findings of this study is available on request from the corresponding author.

Acknowledgements We thank A. Jensenius, O. Jensenius and L. Bisiot for their discovery of the reshaping behaviour of groovy metasheets. We thank H. Bense, C. Coulais, L. Domino, T. Jules, E. Filipov, M. Labousse, B. Overvelde, M. Serra-Garcia, Y. Shokef and A. Schenning for discussions. We are grateful to the precision manufacturing departments at AMOLF and Leiden University's Institute of Physics, and to J. Mesman-Vergeer, D. Ursem and J. Verlinden for technical support.

Author contributions M.v.H. conceived and guided the work, and performed exploratory experiments and simulations. A.S.M. performed experiments, simulations and analytical calculations. M.v.H. and A.S.M. jointly developed the conceptual framework and wrote the manuscript.

Competing interests The authors declare no competing interests.

Additional information

Supplementary information The online version contains supplementary material available at https://doi.org/10.1038/s41586-023-06353-5.

Correspondence and requests for materials should be addressed to A. S. Meeussen.

Peer review information *Nature* thanks the anonymous reviewers who contributed to the peer review of this work.

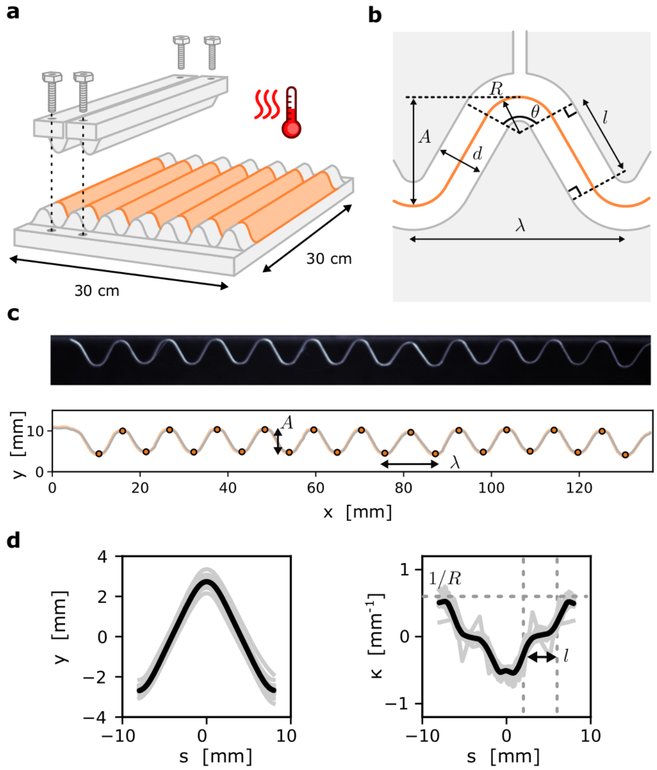

Extended Data Fig. 1 | Groovy sheet fabrication. a, Flat plastic film (orange) is placed on an aluminium mould (grey) with machined grooves. Screw-fastened rods push the film into each groove. **b**, Mould geometry is set by amplitude A, wavelength λ, mean radius R, curve angle θ, facet length l and mould spacing d. The film's mid-surface is indicated (orange line). **c**, Top: cross-section photograph of a 75 μm-thick groovy sheet after forming in the mould (grey line). Bottom: image analysis yields an average amplitude and pitch $A = 5.4 \pm 0.3$ mm and $\lambda = 10.9 \pm 0.3$ mm. **d**, Groove height as a function of arc length s (left) is used to calculate the local curvature κ (right). Averaged values (black lines) yield radius of curvature $R = 2.0 \pm 0.2$ mm and facet length $l = 4.0 \pm 0.1$ mm, close to the mould's shape (dashed lines, $R = 1.5$ mm, $l = 4.4$ mm).

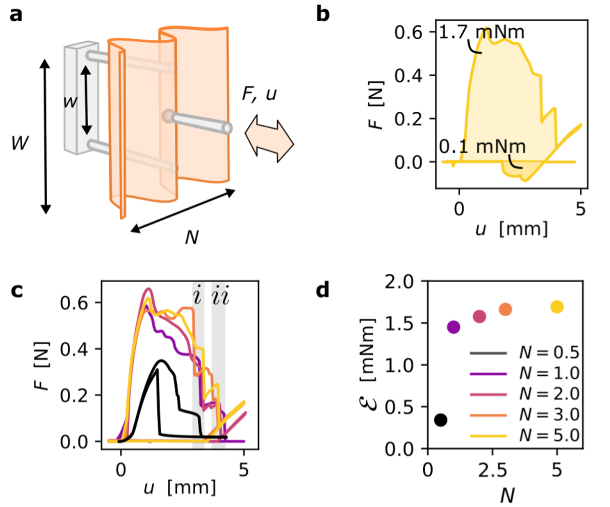

Extended Data Fig. 2 | Popping energy of a single defect. a, Experimental setup. An indenter (grey) is attached by a ball magnet to a sheet (orange, N grooves, width $W = 100 \pm 5\ mm$) and held by two supports at $w = 50\ mm$. Forces F are measured while moving the indenter over displacement u. **b**, Force-displacement curve measured while popping (upper curve) and un-popping (lower curve) a sheet with $N = 5$ grooves. Defect formation corresponds to 1.7 mNm of work (area under curve); un-popping to 0.1 mNm. **c**, Popping of sheets with $N \in [0.5, 1, 2, 3, 5]$. Two snap-through events *i* and *ii* (grey areas) and stable defects are seen for $N = 1$ to 5. Defect at $N = 0.5$ (black curve) is unstable. **d**, Work done during indentation (see **c**) reaches a plateau value around $N = 5$.

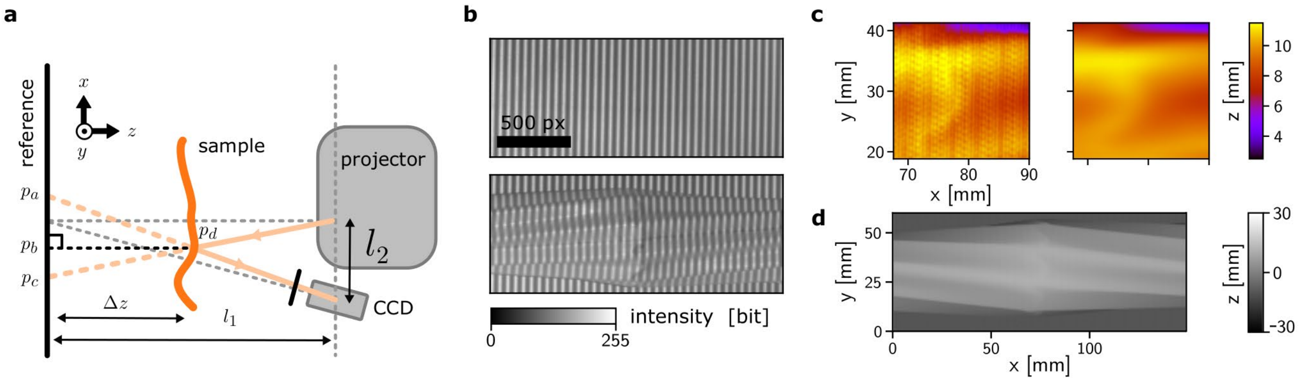

Extended Data Fig. 3 | 3D imaging of groovy sheets. a, A sinusoidal fringe pattern is projected over distance l_1 on a reference plane. The projector's optical axis (grey dashed line) is orthogonal to the reference. A CCD camera (optical axis: grey dashed line) at distance l_2 away from the projector captures the fringe pattern, which may be distorted by a sample (orange lines). **b**, Typical recorded images with and without sample (bottom, top). **c**, Sample height profile (colour bar) is calculated from an image set (left; see main text) and filtered (right). **d**, Typical filtered height profile (colour bar) of a scarred groovy sheet.

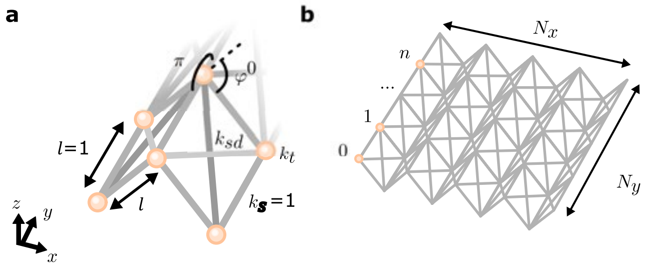

Extended Data Fig. 4 | Computational model of a groovy sheet. a, Unit cell: a square lattice (grey bars) of Hookean edge springs (length $l = 1$, stiffness k_s) cross-braced by diagonal springs (length $\sqrt{2}\,l$, stiffness k_{sd}) and connected by nodes (circles) with torsional hinges (stiffness k_t, resting angle ϕ^0 along $\hat{x}$ and π along $\hat{y}$). **b**, A structure of N_x by N_y nodes mimics a groovy sheet of $N = \frac{N_x - 1}{2}$ grooves. Indices n show node numbering convention.

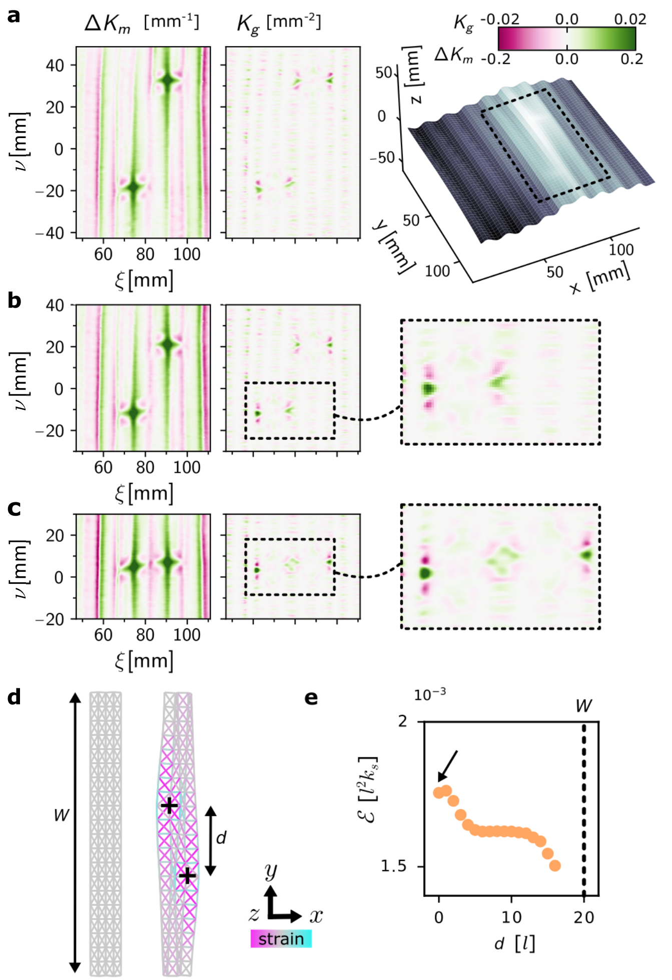

Extended Data Fig. 5 | Experimental and simulated defect interactions. **a**, Experimental differential mean curvature ΔK_m (calculated from difference between surface with and without defects) and Gaussian curvature K_g (colour bar) of a 75 μm-thick groovy sheet with two distant defects in adjacent grooves. ξ, ν are local sheet coordinates. Right: 3D-scan showing region of interest (dashed box). Greyscale indicates z-height. **b**, ΔK_m and K_g for defects at intermediate distance. Zoom-in of K_g shows typical check pattern. **c**, ΔK_m and K_g for bound defects. Zoom-in of K_g shows distinct diamond pattern. **d**, Left: top view of two simulated grooves of length $W = 20l$ where l is the square unit cell size. Right: two defects (plus signs) at mutual distance d, resulting in material strain (colour bar). **e**, Elastic energy $\mathcal{E}$ due to material strain is shown as a function of defect spacing d. A small dip at $d = 0$ is seen (arrow), indicating short-range attraction.

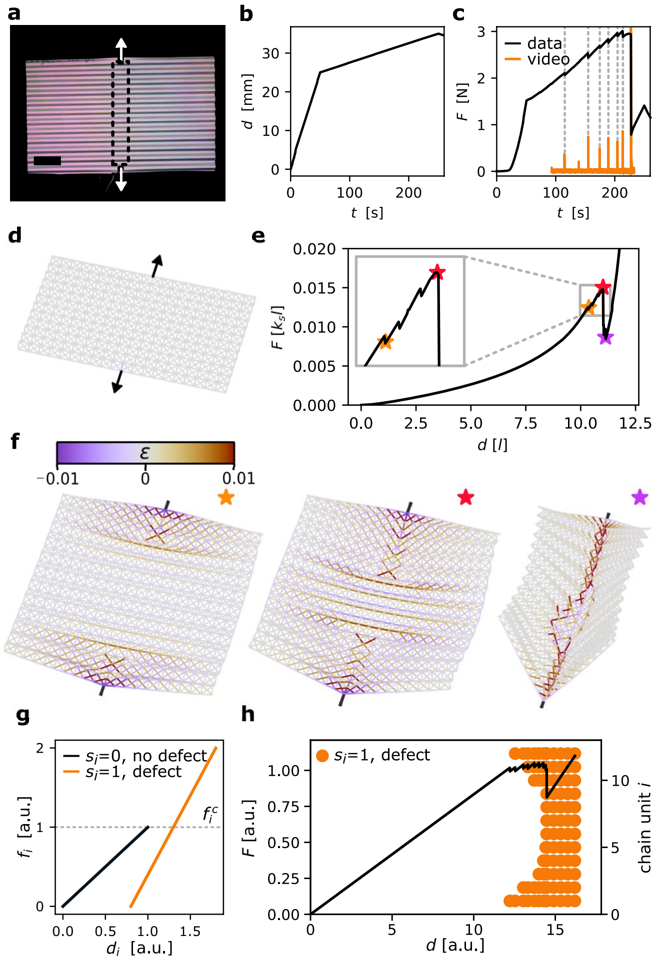

Extended Data Fig. 6 | Scar formation. a, A groovy sheet (14 *cm* wide with 12 grooves, thickness 50 μm, and design wavelength, pitch, and curvature radius $\lambda = 6.2\,mm$, $A = 6.6\,mm$, and $R = 1\,mm$) is attached to an in Instron UTM under point forcing (white arrows). Scale bar: 2 cm. **b**, Applied extension d of the sheet over time t. **c**, Extensional force F as a function of time t (black line). Snapping events are tracked via changes of the video signal (orange line, arbitrary units) within the area shown in **a** (dashed box). Large changes correspond to snapping events (dashed grey lines). **d**, Mimicking the experimental groovy sheet, a numerical model of size $N_x = N_y = 21$ (see Methods) is sequentially extended under point forcing (black arrows). **e**, Numerical force-displacement curve. Minor force drops due to defect nucleation and a major force drop due to sudden scar formation are observed. **f**, Snapshots of the numerical model; corresponding simulation steps are indicated by coloured stars in **e**. Linear spring strain ϵ is shown (colour bar). **g**, Force-displacement curve $f_i(d_i)$ of a theoretical bistable unit i. The unit switches from low-stiffness state $s_i = 0$ (no defect) to high-stiffness state $s_i = 1$ (defect) at critical force f_i^c. **h**, A model of 12 chained bistable units as in **g** is explored (parameters are $f^{c(0)} = 1$, $\lambda = 0.1$, $c = 0.004$, and $p = 2$). Under applied extension, the force F (left axis) and state of each unit is calculated (right axis, legend). Minor force drops correspond to single units switching state, starting at the forcing locations and propagating inward; a major force drop is seen when remaining units avalanche into the defect state.

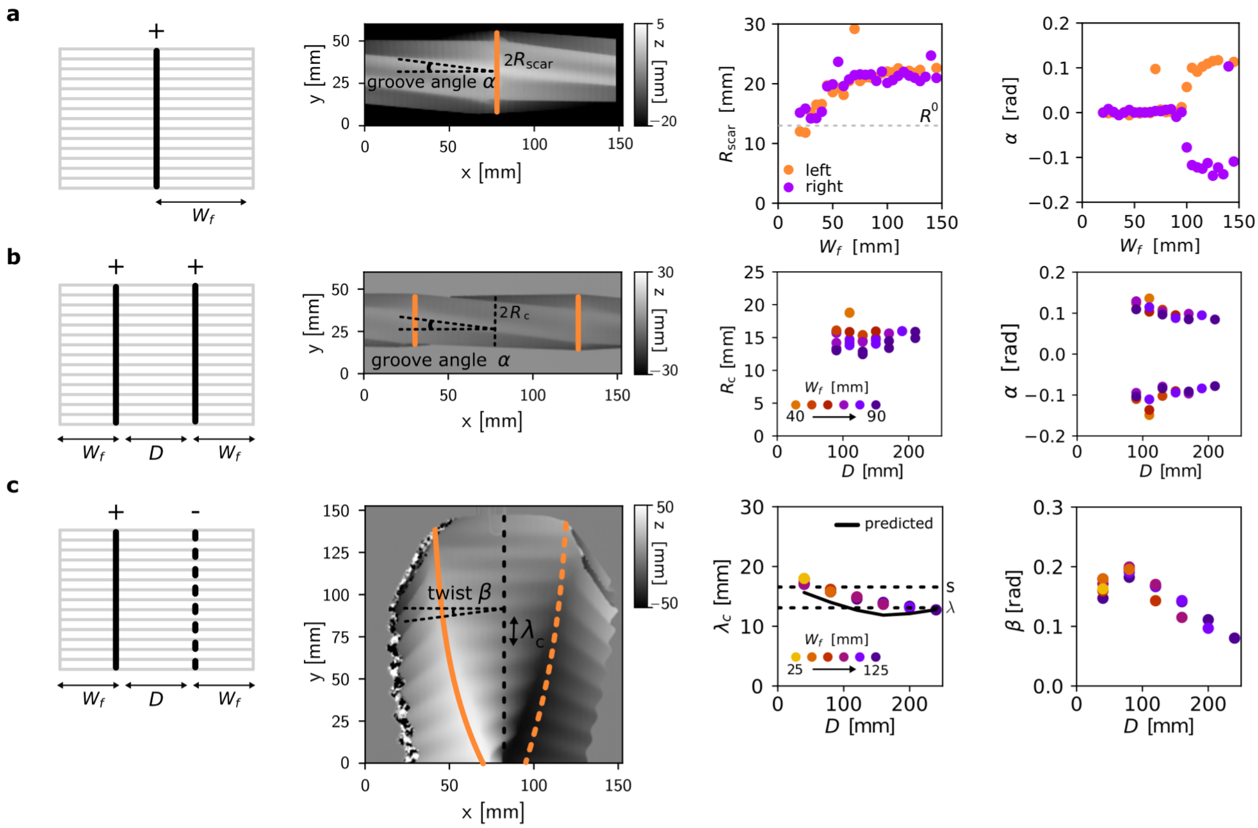

Extended Data Fig. 7 | Shape metrics of 75 μm-thick groovy sheets with one or two scars. a, One scar causes rolling. Left: schematic showing central scar sign and location at distance W_f from sheet edge. Middle: 3D-scanned image of deformed sheet. Shape metrics for twisting (groove angle α) and rolling (scar radius R_{scar}) are indicated. Right: shape metrics measured for increasing scar-edge distance W_f. Saturation of scar radius and a sudden symmetry-breaking twisting bifurcation are observed for increasing W_f. **b**, Two equal-signed scars cause rolling and twisting. Left to right: scar signs and locations at mutual distance D are shown. 3D-scanned image shows groove angle α and central curvature radius R_c. Radius R_c increases weakly with D and decreases weakly with W_f (colors). Groove angle α decreases weakly with D. Note that this configuration is not stable for $D < 90$ mm. **c**, Two opposite-signed scars produce a helical shape. Left to right: scar signs and locations are shown schematically. 3D-scanned image shown shape metrics of twist per groove β and central groove wavelength λ_c. The latter shows a weak decrease with scar-scar distance D and varies between the resting wavelength λ and groove arc length s (dashed lines). Prediction of λ_c for a purely helicoidal shape is shown (solid line, see Eq. (5)). Twist angle β initially increases, then decreases with D. Only left-twisting states are reported; equivalent right-twisting states exist as well.

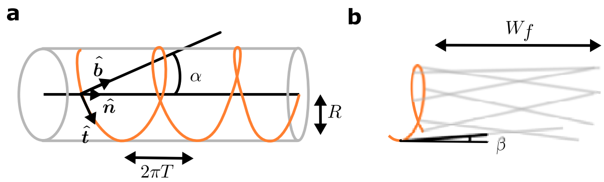

Extended Data Fig. 8 | Ruled surfaces approximate scarred sheet shapes. **a**, A helicoidal base curve of radius R and pitch $2\pi T$ with local coordinate frame $\{\hat{t}, \hat{n}, \hat{b}\}$ (pink line) approximates a scar line. **b**, Straight rules of length W_f extending at an orthogonal angle β away from the base curve (grey lines) approximate the sheet's grooves.

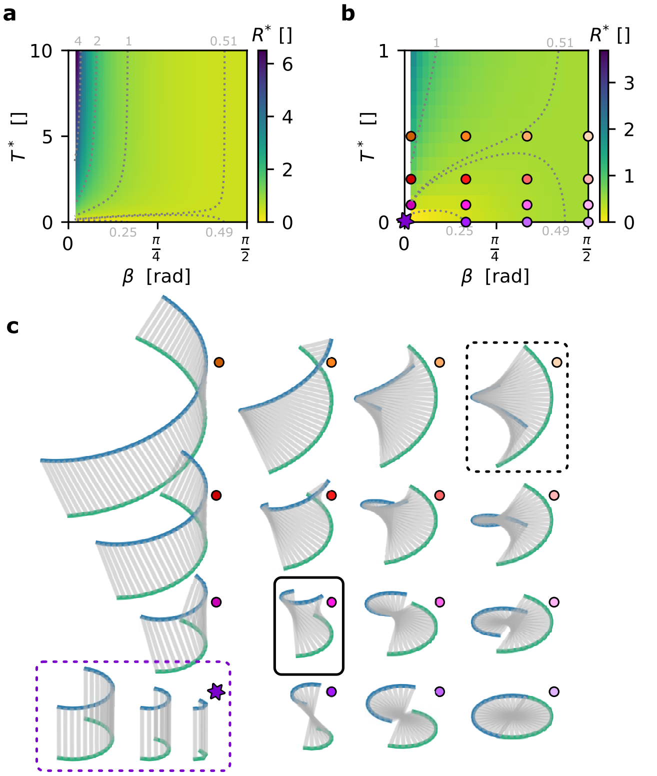

Extended Data Fig. 9 | Admissible sheet shapes for parallel scars in the ruled-surface model. a, State diagram of double-scarred shapes. The rescaled scar radius R^* as function of rescaled pitch T^* and groove angle β is shown (colour bar). Contours of constant R^* are shown for clarity (dashed grey lines). **b**, Zoom-in of experimentally relevant portion of the state diagram. Real sheets with parallel scars exhibit $R^* \lesssim \frac{1}{2}$. **c**, Examples of double-scarred shapes throughout the phase diagram, corresponding to coloured dots in **b**; scar lines (blue/green) and grooves (grey) are indicated. Constant $W_f = 1$ and scar arc length of $\pi/40W_f$ between adjacent grooves were chosen for visualization. Coils (left), cylinders (bottom left), cones (bottom) and helices can be distinguished. Point $T^* = \beta = 0$ produces cylindrical surfaces with arbitrary value of R^* (purple star, dashed box); there are no other surfaces with $\beta = 0$. Solid (dashed) black boxes indicate qualitative experimentally observed shapes for equal (opposite)-parity scars.

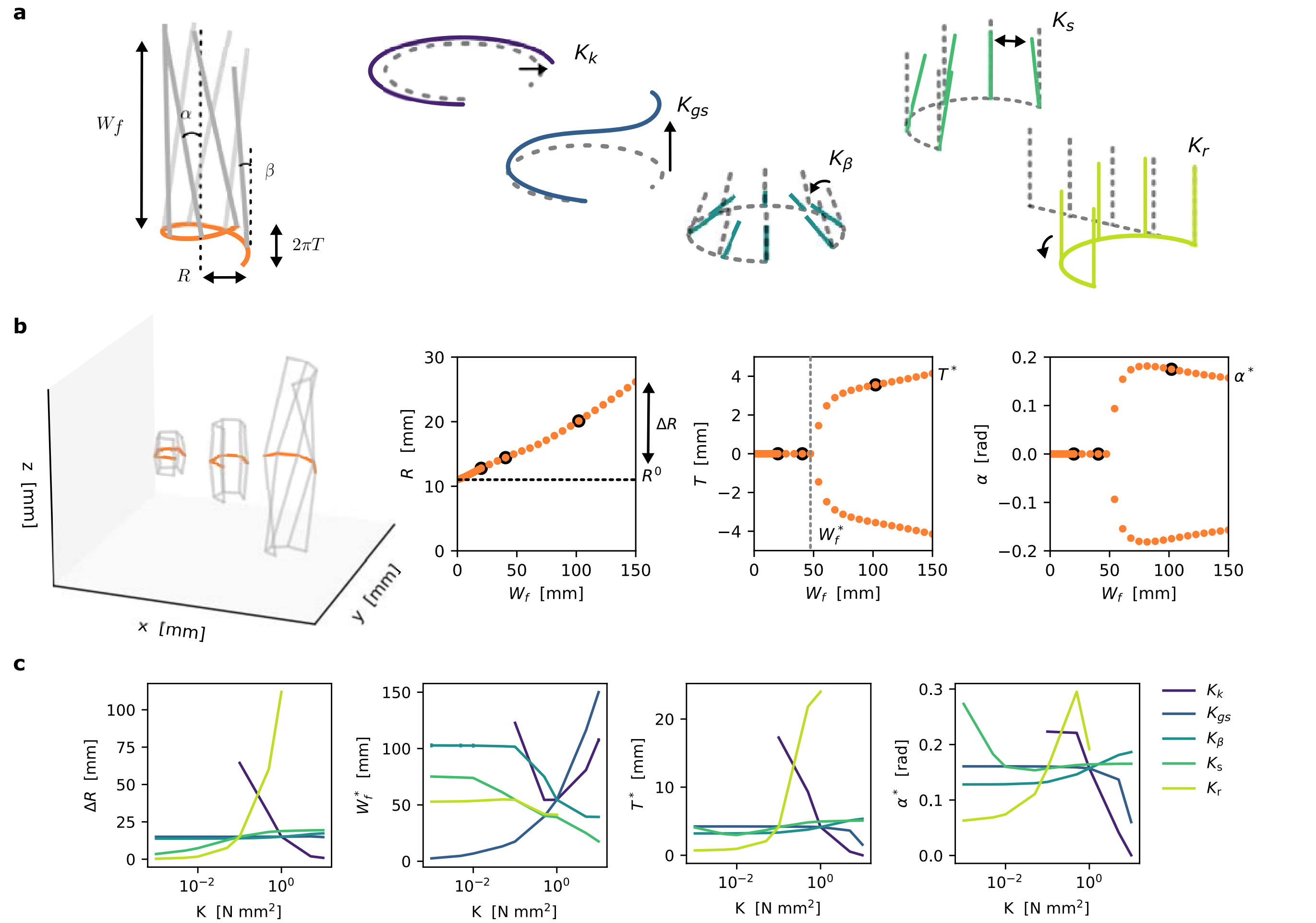

Extended Data Fig. 10 | Twisting transition in a simple elastic model. a, Left: sheets are modelled as ruled surfaces. The scar line forms a helical directrix (orange line) with radius of curvature R_{scar} and pitch $2\pi T$. Grooves (grey lines) are approximated as straight lines of length W_f at angle β to the scar, resulting in a cylindrical shape twisted over angle α. Right: elastic deformation modes of the sheet cost energy (see Eq. (19)) and are resisted with stiffness K_k (scar rolling), K_{gs} (scar torsion), K_β (wing angle changes), K_s (sheet splay), and K_r (sheet rolling). **b**, Energy-minimizing sheet shapes as function of W_f for given deformation resistance $K_k, K_{gs}, K_\beta = 1, K_s, K_r = 0.1$. Consistent with experiments (see Extended Data Fig. 7a), R_{scar} grows from its initial value R^0 by amount ΔR. A twisting bifurcation in T and α is observed at critical W^*_f. Post-bifurcation values T^* and α^* at the end of the studied width range $W_f = 150$ *mm* are indicated. Sheet shapes shown left correspond to black circles in each graph. **c**, The overall sheet shape and existence of the twisting bifurcation, quantified by $\Delta R, W^*_f, T^*$, and α^*, are robust against variations of deformation resistances over several orders of magnitude (legend).